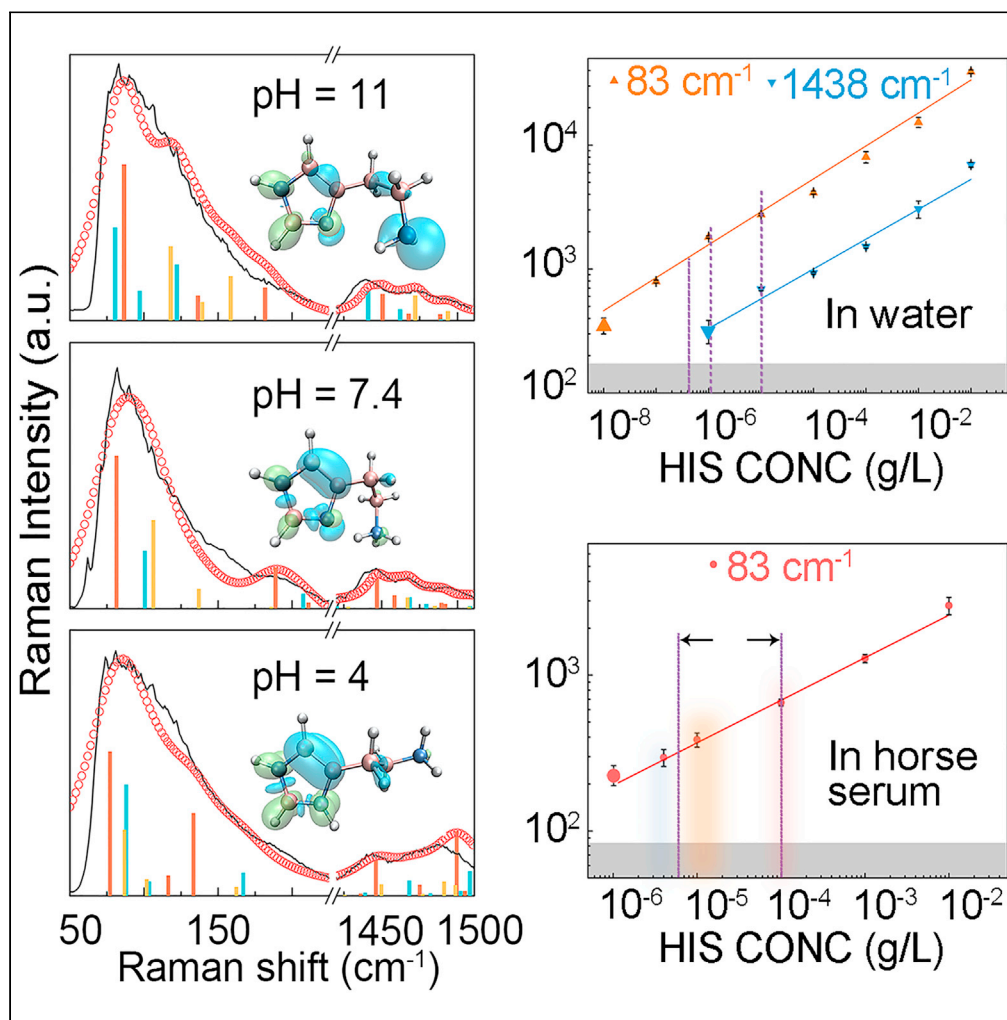**Article**

Strong histamine torsion Raman spectrum enables direct, rapid, and ultrasensitive detection of allergic diseases

Haogang Zhu,
Shuo Liu, Zijing
Guo, ..., Yachong
Guo, Lizhe Liu,
Xinglong Wu

zyzhang@nju.edu.cn (Z.Z.)
yguo@nju.edu.cn (Y.G.)
lzliu@nju.edu.cn (L.L.)
hkxlwu@nju.edu.cn (X.W.)

Highlights

The low-frequency Raman intensity of histamine is stronger than the high-frequency ones

The large Raman intensities arise from torsion vibrations of the C-C single bonds

The detection limit of histamine reaches 10^{-8} g/L in water and 10^{-6} g/L in serum

The whole detection testing only takes less than 20 min

Article

Strong histamine torsion Raman spectrum enables direct, rapid, and ultrasensitive detection of allergic diseases

Haogang Zhu,[1,5] Shuo Liu,[1,5] Zijing Guo,[1,5] Kun Yan,[1] Jiancang Shen,[1] Zhiyong Zhang,[1,*] Jian Chen,[2] Yachong Guo,[1,3,4,*] Lizhe Liu,[1,*] and Xinglong Wu[1,6,*]

SUMMARY

Allergic diseases are closely related to degranulation and release of histamine and difficult to diagnose because non-allergic diseases also exhibit the same clinical symptoms as allergy. Here, we report direct, rapid, and ultrasensitive detection of histamine using low-frequency molecular torsion Raman spectroscopy. We show that the low-frequency (<200 cm^{-1}) Raman spectral intensities are stronger by one order of magnitude than those of the high-frequency Raman ones. Density functional theory calculation and nuclear magnetic resonance spectroscopy identify the strong spectral feature to be from torsions of carbon-carbon single bonds, which produce large variations of the polarizability densities in the imidazole ring and ethyl amino side chain. Using an omniphobic substrate and surface plasmonic effect of Au@SiO$_2$ nanoparticles, the detection limit (signal-noise ratio >3) of histamine reaches 10^{-8} g/L in water and 10^{-6} g/L in serum. This scheme thus opens new lines of inquiry regarding the clinical diagnosis of allergic diseases.

INTRODUCTION

Allergies are the most widely prevalent clinical diseases (Lambrecht and Hammad, 2017; Papadopoulos et al., 2012; Reynolds and Finlay, 2017). Degranulation and release of histamine is a direct cause for allergic symptoms (Akdis and Akdis, 2009; Holgate and Polosa, 2008), so histamine concentration in bodily fluids can serve as a direct allergic indicator, potentially replacing the skin prick test. Currently, detection of histamine concentration is mainly based on biological techniques such as high-performance liquid chromatography (Pittertschatscher et al., 2002), enzyme-linked immunosorbent assay (ELISA) (Nakamura et al., 2017; MacGlashan, 2013), and transgenic cell sensor (Auslander et al., 2014; Chassin et al., 2017). Complex sample preparation, expensive instrumentation, and long inspection time are the main drawbacks of these techniques. Surface-enhanced Raman scattering (SERS) is a useful tool to achieve high-precision detection of small molecules (Giancane et al., 2016; Vander Ende et al., 2019). Determination of histamine concentration in food by SERS in the high-frequency side (>200 cm^{-1}) has been reported recently (Bettini et al., 2019; Huynh et al., 2020). However, the detection limit is higher than 1×10^{-6} g/L and therefore the method can only be used for detecting histamine in food (Filipec et al., 2021; Gao et al., 2015; Janči et al., 2017; Xie et al., 2017). The low intensities of the high-frequency vibrations make invalid the application of SERS in medicine. We carefully checked the low-frequency Raman spectra of histamine molecules in the range of <200 cm^{-1} and clearly observed the high-intensity low-frequency Raman peaks that originate from large variations of the polarizability densities caused by torsions of the C-C bonds in the side chain. Using an omniphobic substrate to concentrate sample and Au@SiO$_2$ nanoparticles (NPs) to provide "hot spots", we reveal the potentials of the surface-enhanced low-frequency Raman scattering (SELFRS) for application in high-precision probe of histamine concentration.

RESULTS AND DISCUSSION

Figure 1A shows 3-dimensional optical photos of the histamine powders exposed in air at 22°C and humidity of 50% for 0, 15, 45, 90, and 135 min. We can see that the powder gradually absorbs water and almost becomes an aqueous solution with 135 min storage in air, indicative of its good hydrophilism. Figure 1B depicts the corresponding room-temperature Raman spectra. For the solid powder, the low-frequency
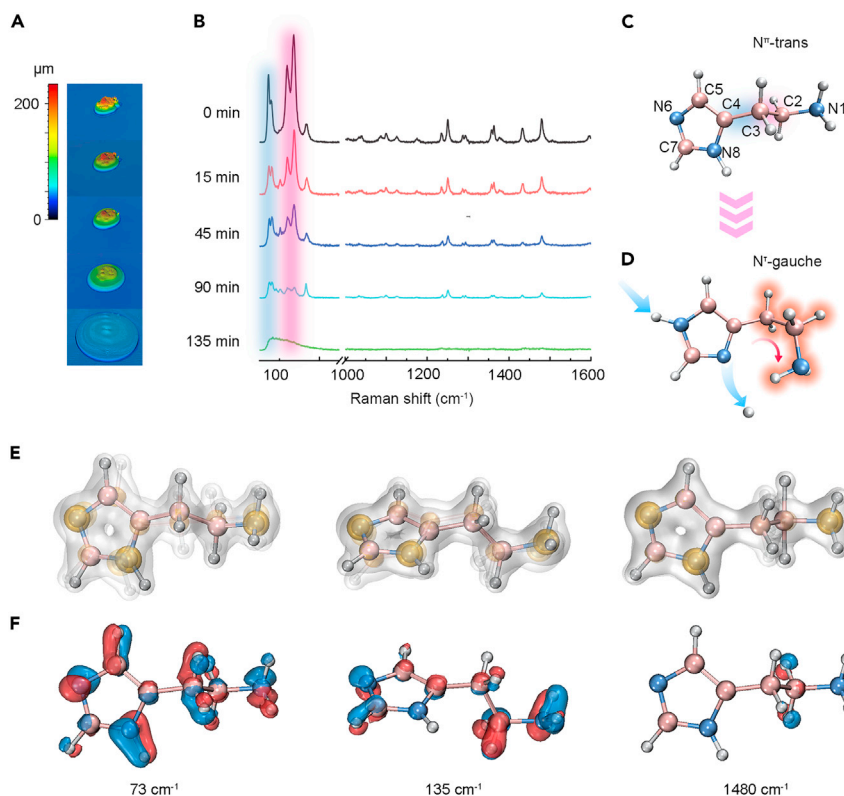
Figure 1. Molecular structure and Raman spectra of histamine

(A and B) Optical photos (A) and Raman spectra (B) of the histamine powders exposed in air at 22°C and 50% humidity for 0, 15, 45, 90, and 135 min. The blue and purple regions in (B) are related to the torsions of the C3-C4 and C2-C3 bonds, respectively.

(C and D) Schematic diagrams of histamine configuration change from solid to aqueous solution. In the solid state, histamine is an N^{π}-trans species (C). With increasing water absorption, histamine gradually transforms into N^{τ}-gauche species (D).

(E and F) Changes of the electron density distributions (E) and Raman polarizability densities (F) for the modes at 73, 135, and 1,480 cm^{-1}. High- and low-electron-density areas are shown in yellow and gray (E), respectively. The polarizability density is normalized and the absolute isovalue is set to 0.15 with the positive signal in blue and the negative in red (F).

side less than 200 cm^{-1} clearly shows six peaks at 73, 79, 103, 119, 135, and 168 cm^{-1} (Figure S1) and the four peaks at 73, 79, 119, and 135 cm^{-1} have the integrated intensities almost higher by one order of magnitude than those in the high-frequency side (Figure S2). The four peaks gradually weaken with increasing water absorption. Interestingly, in the completely dissolved sample with a 135 min absorption duration, these low-frequency peaks merge into a large bump with asymmetric linewidth and the largest intensities appear at the lowest frequency end. Meanwhile, the high-frequency peaks (>200 cm^{-1}) become invisible. It is known that the histamine molecule consists of an imidazole ring and an ethyl amino side chain. The imidazole ring has two N atoms (N6 and N8) and each can attach a proton (Figure 1C). The ethyl amino side chain has an N atom (N1). If only N8 attaches a proton (N^{π}-trans specie), the histamine molecules will form a crystalline structure (Ramírez et al., 2003), which is the case in the solid powder.

With increasing water absorption, the powder slowly dissolves. Partial N6 attaches protons and simultaneously partial N8 loses protons (N^{τ}-gauche species; Figure 1D). Then the histamine molecule changes conformation by forming intramolecular hydrogen bonds instead of interaction with solution molecules (Kodchakorn et al., 2019; Ramírez et al., 2003). This is the case in solutions. Owing to such a special molecular structural evolution, the conformation of histamine is very sensitive to the surrounding environment and causes the torsion of the side chain relative to the imidazole ring to a certain degree (Figure 1D). (Mukherjee and Yadav, 2016; Vianello and Mavri, 2012). Hence, several different conformations could coexist in hydrophil histamine powders. The high-frequency Raman peaks have been observed previously and

assigned to the relative vibrations of various chemical bonds in the histamine molecule (Pittertschatscher et al., 2002). To elucidate the origins of these low-frequency peaks, we performed the combined density functional theory (DFT) calculations by considering the coexistence of several different conformations of histamine in aqueous solution (calculation details in STAR Methods).

For the solid powder, our DFT calculations reveal that the three strongest peaks at 73, 119, and 135 cm^{-1} stem from the torsions of the C3-C4 (the former one) and C2-C3 (the latter two) bonds (Table S1) in the conformation with the dihedral angles θ (C2-C3-C4-C5) and φ (N1-C2-C3-C4) to be 101.6° and 3.7° (Figure S3), respectively. Compared with the high-frequency bending vibration of the H12-C2-H11 bond at 1,480 cm^{-1} (Figure S4), such torsions cause obvious large variations of the electron density distributions (Figures 1E and S5, and Videos S1, S2, S3, and S4) and Raman polarizability densities (Figures 1F and S5) in the imidazole ring and ethyl amino side chain (Raczyńska et al., 2003). Interestingly, our calculations also suggest that the two peaks at 79 and 168 cm^{-1} appear when the histamine molecule absorbs one water molecule to form a hydrogen bond with N6 (Figure S1 and its inset). This indicates that, in the so-called powder sample, some histamine molecules have absorbed a few water molecules when stored in air, and thus the Raman spectrum additionally shows the two new peaks corresponding with the absorption of water molecules. To confirm this inference, we heated the histamine powder under protection of N$_2$ at some set temperatures for 10 min and examined the corresponding Raman spectra. The obtained results show that the two peaks vanish at a measurement temperature of 70°C (Figure S6). Furthermore, when we returned the measurement temperature to the room temperature of 22°C, the two peaks still do not show up. This clearly indicates the role of water molecules. Moreover, we noticed that the 103 cm^{-1} peak with a lower intensity exists in the powder samples with storage times of more than 15 min (Figure 1B). Our calculations indicate that its appearance is also due to the absorption of some water molecules (Figure S1).

The situations in bodily fluids such as blood, nasal mucosa, and gastric mucosa with different pH values are more complicated because of the existence of various biomacromolecules. It is known that histamine has three main ionic forms at different pH environments (Collado et al., 2000; Correa et al., 2007; Nagy et al., 1994), neutral at extremely basic pH, monocation at physiological pH, and dication at acidic pH. Both the neutral and monocation forms are associated with N$^\tau$ species in which the monocation form accepts an additional proton at N1 of the side chain. In the dication form, the three nitrogen atoms all accept protons. The pH value can effectively affect the side-chain internal torsion so as to form stable ionic forms (different torsional isomers) that determine biological activities (Kodchakorn et al., 2019; Mukherjee and Yadav, 2016; Vianello and Mavri, 2012). Figure 2A depicts the low-frequency Raman spectra of the aqueous histamine solutions with three typical pH values of 11, 7.4, and 4. We can clearly observe that the low-frequency peaks all show a large bump with asymmetric linewidth and their intensities are far stronger than those in the high-frequency side. Particularly, we notice that these bumps are stronger at the lowest wavenumber end, indicating that the torsion of the C3-C4 bond is more drastic than that of the C2-C3 bond in the internal torsion of the side chain.

The physicochemical properties of histamine are closely related to its conformation, especially the dihedral angles θ and φ, which allow multiple structures with varying degrees of stability (Table S2). Multiple conformations are responsible for the currently observed low-frequency bump-like Raman spectra because of the flexible tail chain (Katsoulidis et al., 2019). To fit these bumps and seek possible optimal conformations, we searched for the conformational energy landscape as functions of the dihedral angles θ and φ using the DFT B3LYP method (see STAR Methods) (Wang et al., 2019). We determined core conformations and metastable states at basins over the energy landscape as the most possible structures. To ensure a full description of all low-energy conformers, the conformational spaces of histamine corresponding with accurate estimates of energy were explored by considering all possible combinations of various torsional degrees of the C2-C3 and C3-C4 bonds. The 3D presentations of the energy landscapes are shown in Figure 2B for the three different pH histamine solutions. Three energy minima in each landscape were selected as three stable states of the histamine molecule in each pH solution. We calculated the local nucleophilicity and electrophilicity of these minimum energy conformations by orbital-weighted Fukui functions (Figure 2C; Felten et al., 2015) and found that the surrounding of N8 is nucleophilic (bluer) in the neutral/monocation forms and electrophilic (greener) in the dication form. This indicates that the neutral/monocation forms are more likely to form intramolecular hydrogen bonds to bend the internal side chain than the dication form. Based on the molecular conformation of each stable state with the minimum energy, we calculated the corresponding Raman spectra and found that each conformation is associated with three Raman peaks in the low-frequency side and the highest intensity peak appears at the lowest wavenumber end associated
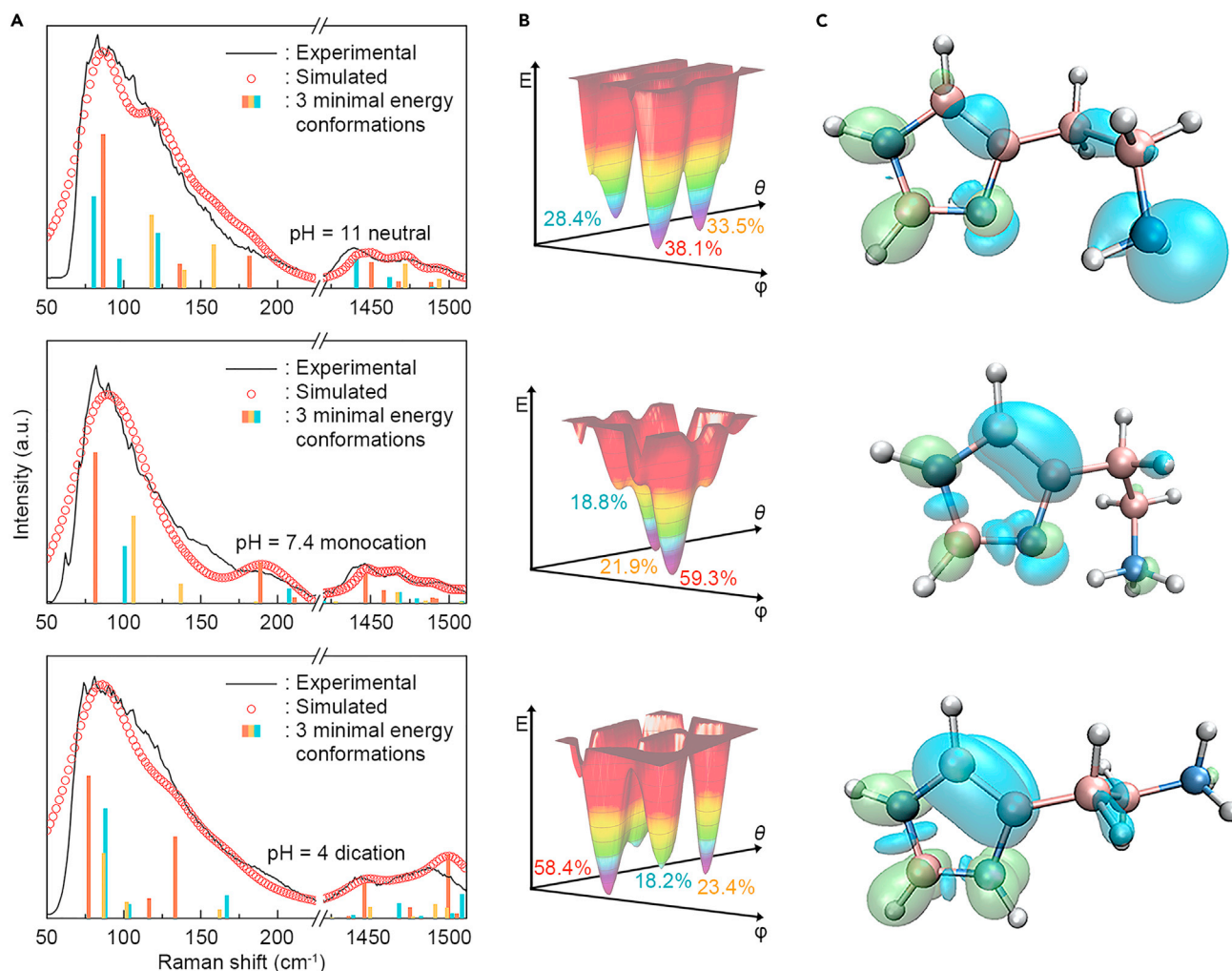
Figure 2. pH-mediated histamine conformational transition

(A) Experimental (black) and simulated (red) Raman spectra acquired from three different pH histamine solutions (0.1 M). These solutions are prepared using 0.1 M NaOH solution for pH = 11 and 0.1 M hydrochloric acid for pH = 7.4 and 4. Red, yellow, and blue columns illustrate the calculation Raman peaks of three minimum energy conformations, which correspond to the three lowest points in (B).

(B) Landscapes of the histamine structures in three different pH solutions (a representation of energy, E, as functions of the dihedral angles θ and φ of histamine molecule). The ratios of the three minimum energy conformations are indicated in three colors.

(C) Local nucleophilicity (blue) and electrophilicity (green) of the calculated minimum energy conformation, which correspond to the lowest point in (B).

with the torsion of the C3-C4 bond (Figure 2A). Least-squares analysis was used to quantitatively determine the relative ratios of the three minimal energy conformations (Willoughby et al., 2014). According to the ratios, we can get simulations via linear superimposing of the calculated Raman spectra of each conformation. The theoretical results fit very well the observed experiments in both the low- and high-frequency sides (Figure 2A and Table S2).

To check the correctness of the three minimum energy conformations in each pH solution, we calculated the chemical shifts of all C atoms based on the relative ratios of the three minimum energy states (Chen et al., 2019) and compared these results with the corresponding experimental values from the ^{13}C nuclear magnetic resonance (NMR) spectra (Figure 3A). As shown in Figures 3B–3D, the calculated chemical shifts of the five C atoms (C2–C5 and C7) in the three kinds of histamine solutions with pH of 11, 7.4, and 4 are almost equal to the experimental values with the coefficient of determination R (Lambrecht and Hammad, 2017) of approximately 1. This indicates that the histamine molecules in each pH solution mainly occur with the three minimal energy conformations. We also calculated the changes of the electron density distributions
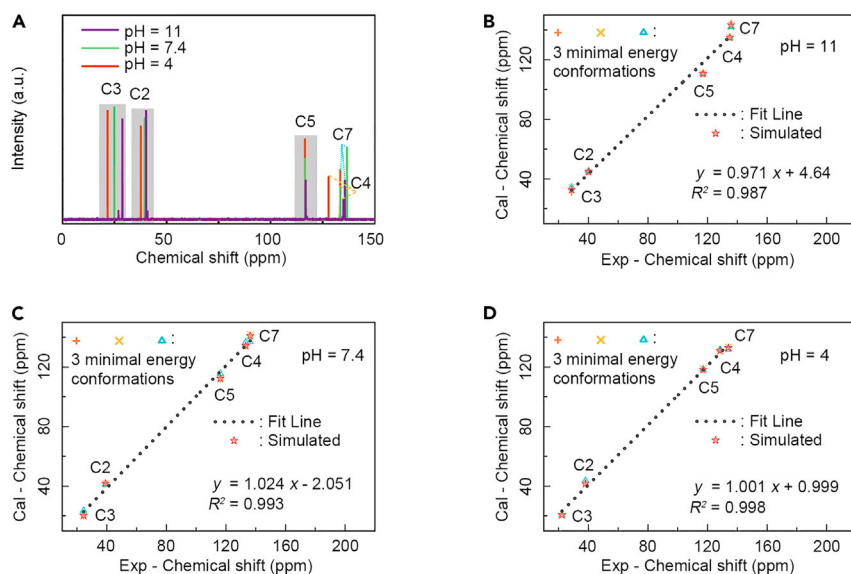
Figure 3. ^{13}C NMR spectra and chemical shifts of C atoms

(A) ^{13}C NMR spectra of the histamine solutions with pH = 11, 7.4, and 4.

(B–D) Comparison between the experimental (horizontal axis) and DFT-computed (vertical axis) ^{13}C NMR chemical shifts of the three minimum energy conformations from the histamine solutions of pH = 11 (B), 7.4 (C), and 4 (D).

and Raman polarizability densities for the lowest wavenumber peak of the minimum energy conformation and found that they are still more dramatic for the torsion of the C3-C4 bond than those for the bending vibration of the H14-C3-H13 bond in the high-frequency side (Figures S7 and S8). Furthermore, we calculated the corresponding low- and high-frequency Raman scattering activities S_i determined by the polarizability derivative (computational details in STAR Methods) (Chen et al., 2019). According to the obtained S_i and peak frequency, we calculated the integrated intensity I_i of the lowest wavenumber peak in each minimum energy conformation and found that it is about 5 times as much as that of the high-wavenumber peak (Figure S7). Considering the contribution from the other two minimal energy conformations, it is obvious to have the low-frequency Raman intensity far stronger than the high-frequency one.

Increasing histamine concentration would cause different allergic symptoms in different organs (Lambrecht and Hammad, 2017; Yu et al., 2016), particularly in blood. Thus, we can diagnose whether a patient is allergic by examining the low-frequency Raman signal. The strong low-frequency Raman scattering provides a possibility for detecting histamine concentration in various liquid environments. Here, we develop a fast, direct, and low-cost method to realize high-precision detection of histamine concentration using a SELFRS substrate that consists of an omniphobic surface (Li et al., 2010; Wong et al., 2011) and Au@SiO$_2$ NPs. The omniphobic surface is used to concentrate samples, and the Au@SiO$_2$ NPs provide dramatically localized electromagnetic enhancement to amplify the Raman signal. We can notice here that the chemical interaction between the analyte and Au NPs is negligible because the thin layer of SiO$_2$ on Au NPs separates the NPs from direct contact with the probed molecules. The preparation of the SELFRS substrate is described in supplemental information and Figures S9–S17. Our rhodamine 6G (R6G) Raman signal test shows that the enhancement factor on our fabricated SELFRS substrate reaches 1.0×10^6 and no significant low-frequency Raman signal (<200 cm^{-1}) is observed (Figure S15). To practically detect histamine concentration, we may take a few milliliters of blood from the patient and then process through the following steps. The whole testing process only takes less than 20 min.

Step one: Centrifuge blood in an ultrafiltration spin column (molecular weight cutoff = 3 kDa) at 4,000 g for 5 min to remove biomacromolecules in the blood and obtain the serum at the bottom of the column. Then add Au@SiO$_2$ NPs to the serum to obtain uniform miscible liquids after ultrasonic vibration (Figure 4A).

The serum and Au@SiO$_2$ NPs are mixed in a volume ratio of 1:3. The Au@SiO$_2$ NPs have strong surface plasma, which can effectively enhance the Raman signals of neighboring detected molecules (Ding
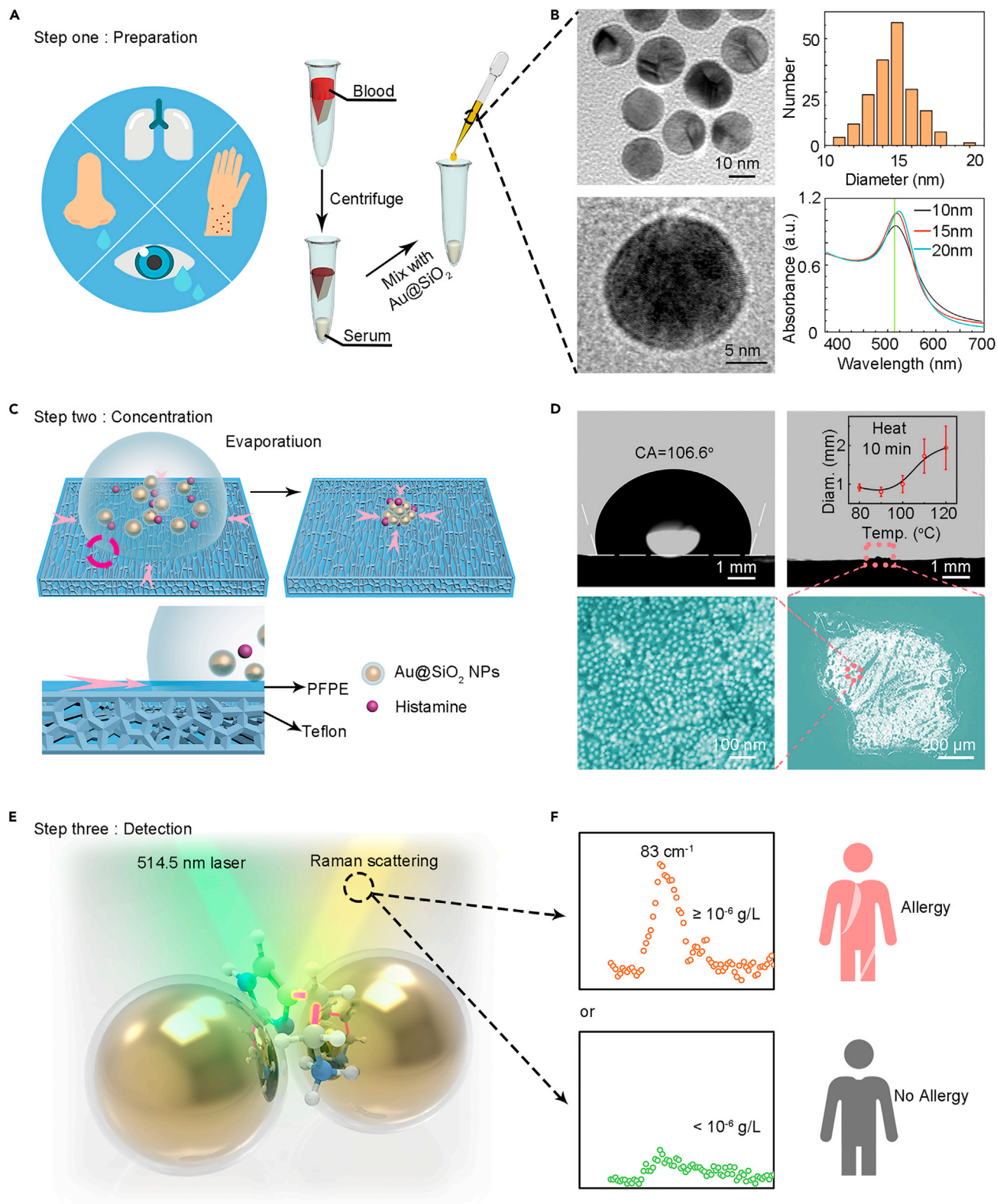
Figure 4. High-precision detection of histamine concentration

(A) Step one: Preparation. Description of several common allergic symptoms (left) and extraction of the serum as well as its mixture with Au@SiO₂ NPs (right).

Figure 4. Continued

(B) TEM images (left) and size distribution (top right) of the used Au@SiO$_2$ NPs. The bottom right shows the UV-vis absorption spectra of the Au@SiO$_2$ NPs with three different sizes. The vertical green line marks the wavelength at 514.5 nm.

(C) Step two: Concentration. The histamine/serum/Au@SiO$_2$ NPs mixture is enriched on an omniphobic surface to obtain a stronger Raman signal via surface plasmonic resonance.

(D) Optical photograph of the contact angle of a histamine/serum/Au@SiO$_2$ NPs mixture on an omniphobic substrate surface (top left). After evaporation, small aggregate forms (top right, the inset shows the dependence of aggregate diameter on the temperature of evaporation). SEM images with low and high magnifications of the small aggregate surface are shown in the bottom right and left, respectively.

(E) Step three: Detection. Schematic representation of the locally enlarged aggregate structure and Raman scattering measurement.

(F) Schematic diagram of the low-frequency Raman spectrum for an allergic case. No low-frequency Raman peak is observed for a non-allergic case.

et al., 2017). The size and structure of the Au@SiO$_2$ NPs used are specially designed to have the plasmonic resonance with the incident light of the 514.5-nm line from an Ar$^+$ laser (Figure S12). Here, the ultra-thin silica shell serves as an isolated layer protecting direct contact from surrounding histamine molecules (Figure S9) (Li et al., 2010). The bottom right in Figure 4B presents the ultraviolet-visible (UV-vis) absorption spectra of the Au@SiO$_2$ NPs with different sizes. The three kinds of Au@SiO$_2$ NPs have plasmonic absorption peaks close to the wavelength of the used laser line at 514.5 nm and the optimal sizes should be 15 nm (top right). The left side in Figure 4B depicts the transmission electron microscope (TEM) images of the Au@SiO$_2$ NPs. The surface silica thin layer with a thickness of less than 1 nm can be observed clearly, which ensures the largest plasmonic resonance strength to occur at the Au@SiO$_2$ NP surface for effectively enhancing the Raman scattering intensity of the absorbed molecules (Figure S18; (Ding et al., 2017).

Step two: Concentrate the miscible liquids. Forty microliters of the miscible liquids is dripped onto an omniphobic surface to eliminate the coffee-ring effect, which occurs when a biological solution sample is dried (Figure 4C). The contact angle of 106.6° indicates an omniphobicity of the substrate surface (top left in Figure 4D). After being heated at 90°C for 10 min (inset of the top right in Figure 4D), the miscible liquids are concentrated to form a small-sized aggregate (top right in Figure 4D). The scanning electron microscope (SEM) images of the small aggregate are shown in the bottom in Figure 4D. Uniform distribution of the Au@SiO$_2$ NPs can be observed clearly.

Step three: Examine the low-frequency Raman spectrum of the small aggregate and make diagnosis (Figure 4E). For an allergic sample, a low-frequency Raman signal with the strongest peak position at about 83 cm^{-1}, which depends on the level of allergy, is observed possibly (Figure 4F).

To confirm the feasibility of the aforementioned examination steps, we experimentally prepared some histamine-water solutions adjusted to pH 7.4 with a buffer (phosphate-buffered saline) for simulating the serum environment at different histamine concentrations. Using the aforementioned SELFRS substrate, the corresponding surface-enhanced low- and high-frequency Raman spectra are obtained and shown in Figures 5A and 5B, respectively. The orange and blue vertical dotted lines mark the positions of the strongest low- and high-frequency peaks at 83 and 1,438 cm^{-1}, respectively. With decreasing concentration of histamine, the intensities of the two peaks gradually decrease. The dependence of intensity on histamine concentration is depicted in Figure 5C. Compared with the fluorometric assay, the high-frequency Raman detection is of higher precision and reaches 10^{-6} g/L (Douabale et al., 2003; Yadava et al., 2019), but it is lower by one order of magnitude than the value obtained from the commercial ELISA kit (Figure S19). However, using the low-frequency Raman detection, the histamine concentration can reach 10^{-8} g/L with a precision higher by one order of magnitude than the result using the commercial ELISA kit. The complex environment in biological samples may affect the accuracy of all detection methods. To validate the effectiveness of this method, we examined a practical situation using a horse serum sample. According to the aforementioned processing steps, different concentrations of histamine were added to the horse serum. The SELFRS results were acquired and depicted in Figure 5D. The vertical red dotted line marks the position of the strongest low-frequency Raman peak at 83 cm^{-1}, and the dependence of its intensity on histamine concentration is shown in Figure 5E. We can see that the linearity range of this method in the horse serum is wider than that using the commercial ELISA kit, essentially meeting diagnostic requirements for different degrees of allergy caused by, for example, cardiac arrest, bronchospasm, and urticaria.

Conclusions

Histamine and some histamine-like molecules with a ringed group and carbon side chain such as dopamine, serotonin, and adrenaline represent a species of important neurotransmitters (Chen et al., 2019;
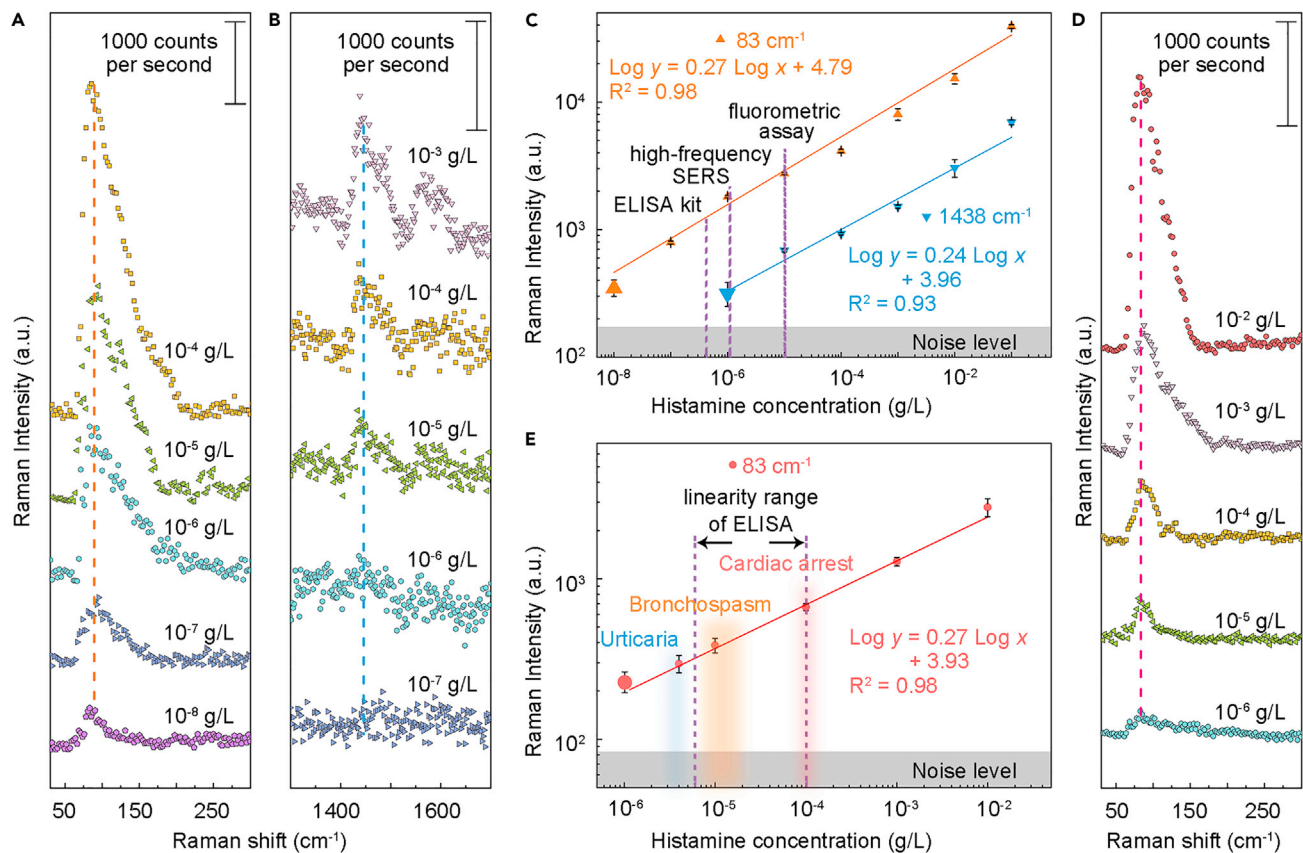
Figure 5. Analysis and comparison of detection precisions for histamine concentrations

(A and B) Low- (A) and high-frequency (B) surface-enhanced Raman scattering (SERS) spectra of the histamine-buffer solutions with different histamine concentrations at pH = 7.4.

(C) Intensities of the low- (83 cm^{-1}, orange dots) and high-frequency (1,438 cm^{-1}, blue dots) Raman peaks versus histamine concentration. The two enlarged orange and blue dots mark the detection limits. Three vertical purple dotted lines mark the detection limits of three common histamine detection techniques (fluorometric assay, high-frequency SERS, and commercial ELISA kit).

(D) SELFRS spectra of the histamine/horse serum solutions with different histamine concentrations at pH = 7.4.

(E) Intensity of the low-frequency Raman peak (83 cm^{-1}, red dots) versus histamine concentration. The enlarged red dot marks the detection limits. The regions of three colored rectangles indicate the levels of histamine concentrations in the human serums caused by cardiac arrest, bronchospasm, and urticaria. The concentration range between two vertical purple dotted lines indicates the detection region by commercial ELISA kits in the horse serums. Data are represented as mean ± SEM.

Panula and Nuutinen, 2013; Shan et al., 2015) that play a significant role in human immune, cardiovascu- lar, central nervous, and hormonal systems. Direct, rapid, and high-precision probing of their concentra- tions is beneficial to early diagnosis of many diseases such as Parkinson's reaction, myocardial infarction, serotonin syndrome, depression, Tourette syndrome, asthma, and autoimmune diseases. It may be possible to increase their detection limits by examining the high-intensity low-frequency torsion Raman spectra of C-C bonds in the side chain on a SERS substrate. In this work, we decrease the detection limit of histamine to 1×10^{-6} g/L in serum by making use of SELFRS spectra, which can meet the requirements of allergy diagnosis. A combination of this scheme with other probing techniques may allow better determination of the existence of related diseases and thus run reasonable and resultful therapy.

Limitations of the study

Although the experimental process has been highly simplified, it is necessary that the tester has experience in instrument operation to obtain good measurement results. This work has only been verified in horse serum and the clinical trials are lacking.

STAR★METHODS

Detailed methods are provided in the online version of this paper and include the following:

- KEY RESOURCES TABLE
- RESOURCE AVAILABILITY
  - Lead contact
  - Materials availability
  - Data and code availability
- METHOD DETAILS
  - Raman spectral examinations
  - 3D-FDTD numerical method
  - Computational details
  - Syntheses of Au NPs with different sizes and associated Au@SiO$_2$ NPs
  - Preparation of omniphobic substrates
  - Immunoassay reagents, equipment and procedure
- QUANTIFICATION AND STATISTICAL ANALYSIS
  - Statistical significance
  - Detection limit calculation

SUPPLEMENTAL INFORMATION

Supplemental information can be found online at https://doi.org/10.1016/j.isci.2021.103384.

AUTHOR CONTRIBUTIONS

H.Z. performed the experiments, analyzed the data, and co-wrote the manuscript. S.L., Z.G., and K.Y. performed partial experiments. J.S. performed the Raman measurements. J.C. analyzed the data. Z.Z., Y.G., and L.L. performed the theoretical calculations and co-wrote the manuscript. X.W. initiated the project, analyzed the data, and wrote the manuscript.

DECLARATION OF INTERESTS

The authors declare no competing interests.

REFERENCES

Akdis, M., and Akdis, C.A. (2009). Therapeutic manipulation of immune tolerance in allergic disease. Nat. Rev. Drug Discov. 8, 645–660.

Auslander, D., Eggerschwiler, B., Kemmer, c., Geering, b., Ausländer, S., and Fussenegger, M. (2014). A designer cell-based histamine-specific human allergy profiler. Nat. Commun. 5, 4408.

Barone, V., Cossi, M., and Tomasi, J. (1998). Geometry optimization of molecular structures in solution by the polarizable continuum model. J. Comp. Chem. 19, 404–417.

Bettini, S., Pal, S., Sawalha, S., Licciulli, A., Valli, L., Giancane, G., and Pagano, R. (2019). Cellulose-based substrate for SERS-promoted histamine

picomolar detection in beverages. ChemistrySelect 4, 2968–2975.

Chassin, H., Geering, B., Schukur, L., Ausländer, D., Lang, B., and Fussenegger, M. (2017). Sensing and responding to allergic response cytokines through a genetically encoded circuit. Nat. Commun. 8, 1101.

Chen, X., Liu, P.C., Hu, Z.W., and Jensen, L. (2019). High-resolution tip-enhanced Raman scattering probes sub-molecular density changes. Nat. Commun. 10, 2567.

Collado, J.A., Tuñón, I., Silla, E., and Ramírez, F.J. (2000). Vibrational dynamics of histamine monocation in solution: an experimental (FT-IR,

FT-Raman) and theoretical (SCRF-DFT) study. J. Phys. Chem. A 104, 2120–2131.

Correa, J.V., Herrera, B., and Toro-Labbé, A. (2007). Characterization of the reactive conformations of protonated histamine through the reaction force analysis and the dual descriptor of chemical reactivity. J. Mol. Struct. Theochem. 817, 111–118.

Ding, S.Y., You, E.M., Tian, Z.Q., and Moskovits, M. (2017). Electromagnetic theories of surface-enhanced Raman spectroscopy. Chem. Soc. Rev. 46, 4042–4076.

Douabale, S.E., Dione, M., Coly, A., and Tine, A. (2003). Contributions to the determination of histamine rate by measuring out the

histamine-orthophthalaldehyde complex in the absorption and fluorescence. Talanta 60, 581–590.

Felten, J., Hall, H., Jaumot, J., Tauler, R., Juan, A.D., and Gorzsás, A. (2015). Vibrational spectroscopic image analysis of biological material using multivariate curve resolution-alternating least squares (MCR-ALS). Nat. Protoc. 10, 217–240.

Filipec, S.V., Valinger, D., Mikac, L., Ivanda, M., Kljusurić, J.G., and Jančı, T. (2021). Influence of sample matrix on determination of histamine in fish by surface enhanced Raman spectroscopy coupled with chemometric modelling. Foods 10, 1767.

Gao, F., Grant, E., and Lu, X.N. (2015). Determination of histamine in canned tuna by molecularly imprinted polymers-surface enhanced Raman spectroscopy. Anal. Chim. Acta 901, 68–75.

Giancane, G., Bettini, S., Pagano, R., and Valli, L. (2016). ZnO-porphyrin composite nanostructures as discriminating adducts for metallic ions in aqueous matrices. ChemistrySelect 1, 4690–4695.

Holgate, S.T., and Polosa, R. (2008). Treatment strategies for allergy and asthma. Nat. Rev. Immunol. 8, 218–230.

Huynh, K., Pham, X., Hahm, E., An, J., Kim, Y., Jo, A., Seong, B., Kim, Y., Son, B.S., Kim, J., et al. (2020). Facile histamine detection by surface-enhanced Raman scattering using SiO_2@Au@Ag alloy nanoparticles. Int. J. Mol. Sci. 21, 4048.

Jančı, T., Valinger, D., Kljusurić, J.G., Mikac, L., Vidaček, S., and Ivanda, M. (2017). Determination of histamine in fish by surface enhanced Raman spectroscopy using silver colloid SERS substrates. Food Chem. 224, 48–54.

Katsoulidis, A.P., Antypov, D., Whitehead, G.F.S., Carrington, E.J., Adams, D.J., Berry, N.G., Darling, G.R., Dyer, M.S., and Rosseinsky, M.J. (2019). Chemical control of structure and guest uptake by a conformationally mobile porous material. Nature 565, 213–217.

Kodchakorn, K., Nimmanpipug, P., Phongtamrug, S., and Tashiro, K. (2019). pH-induced conformational changes in histamine in the solid state. RSC Adv. 9, 19375–19389.

Lambrecht, B.N., and Hammad, H. (2017). The immunology of the allergy epidemic and the hygiene hypothesis. Nat. Immunol. 18, 1076–1083.

Li, J.F., Huang, Y.F., Ding, Y., Yang, Z.L., Li, S.B., Zhou, X.S., Fan, F.R., Zhang, W., Zhou, Z.Y., Wu, D.Y., et al. (2010). Shell-isolated nanoparticle-enhanced Raman spectroscopy. Nature 464, 392–395.

MacGlashan, D.W. (2013). Basophil activation testing. J. Allergy Clin. Immunol. 132, 777–787.

Mennucci, B., Tomasi, J., Cammi, R., Cheeseman, J.R., Frisch, M.J., Devlin, F.J., Gabriel, S., and Stephens, P.J. (2002). Polarizable continuum model (PCM) calculations of solvent effects on optical rotations of chiral molecules. J. Phys. Chem. A. 106, 6102–6113.

Mukherjee, V., and Yadav, T. (2016). Conformational study of neutral histamine monomer and their vibrational spectra. Spectrochim. Acta A Mol. Biomol. Spectrosc. 165, 167–175.

Nagy, P.I., Durant, G.J., Hoss, W.P., and Smith, D.A. (1994). Theoretical analyses of the tautomeric and conformational equilibria of histamine and (.alpha.R,.beta.S)-.alpha.,.beta.-Dimethylhistamine in the gas phase and aqueous solution. J. Am. Chem. Soc. 116, 4898–4909.

Nakamura, Y., Ishimaru, K., Shibata, S., and Nakao, A. (2017). Regulation of plasma histamine levels by the mast cell clock and its modulation by stress. Sci. Rep. 7, 39934.

Panula, P., and Nuutinen, S. (2013). The histaminergic network in the brain: basic organization and role in disease. Nat. Rev. Neurosci. 14, 472–487.

Papadopoulos, N.G., Agache, I., Bavbek, S., Bilo, B.M., Braido, F., Cardona, V., Custovic, A., deMonchy, J., Demoly, P., Eigenmann, P., et al. (2012). Research needs in allergy: an EAACI position paper, in collaboration with EFA. Clin. Transl. Allergy 2, 21.

Pittertschatscher, K., Hochreiter, R., Thalhamer, J., and Hammerl, P. (2002). Quantification of histamine in blood plasma and cell culture supernatants: a validated one-step gas chromatography-mass spectrometry method. Anal. Biochem. 308, 300–306.

Podstawka-Proniewicz, E., Andrzejak, M., Kafarski, P., Kim, Y., and Proniewicz, L.M. (2011). Vibrational characterization of L-leucine phosphonate analogues: FT-IR, FT-Raman, and SERS spectroscopy studies and DFT calculations. J. Phys. Chem. A 42, 958–979.

Raczyńska, E.D., Darowska, M., Cyrański, M.K., Makowski, M., Rudka, T., Gal, J.-F., and Maria, P.-C. (2003). Ab initio study of tautomerism and of basicity center preference in histamine, from gas phase to solution-comparison with experimental data (gas phase, solution, solid state). J. Phys. Org. Chem. 16, 783–796.

Ramírez, F.J., Tuñón, I., Collado, J.A., and Silla, E. (2003). Structural and vibrational study of the tautomerism of histamine free-base in solution. J. Am. Chem. Soc. 125, 2328–2340.

Reynolds, L.A., and Finlay, B.B. (2017). Early life factors that affect allergy development. Nat. Rev. Immunol. 17, 518–528.

Shan, L., Dauvilliers, Y., and Siegel, J.M. (2015). Interactions of the histamine and hypocretin systems in CNS disorders. Nat. Rev. Neurol. 11, 401–413.

Vander Ende, E., Bourgeois, M.R., Henry, A., Chavez, J.L., and Krabacher, R. (2019). Physicochemical trapping of neurotransmitters in polymer-mediated gold nanoparticle aggregates for surface-enhanced Raman spectroscopy. Anal. Chem. 91, 9554–9562.

Vianello, R., and Mavri, J. (2012). Microsolvation of the histamine monocation in aqueous solution: the effect on structure, hydrogen bonding ability and vibrational spectrum. New J. Chem. 36, 954–962.

Wang, B., Rong, C.Y., Chattaraj, P.K., and Liu, S.B. (2019). A comparative study to predict regioselectivity, electrophilicity and nucleophilicity with Fukui function and hirshfeld charge. Theor. Chem. Acc. 138, 124.

Weijo, V., Mennucci, B., and Frediani, L. (2010). Toward a general formulation of dispersion effects for solvation continuum models. J. Chem. Theor. Comput. 6, 3358–3364.

Willoughby, P., Jansma, M., and Hoye, T. (2014). A guide to small-molecule structure assignment through computation of (1H and 13C) NMR chemical shifts. Nat. Protoc. 9, 643–660.

Wong, T.S., Kang, S.H., Tang, S.K.Y., Smythe, E.J., Hatton, B.D., Grinthal, A., and Aizenberg, J. (2011). Bioinspired self-repairing slippery surfaces with pressure-stable omniphobicity. Nature 477, 443–447.

Xie, Z.J., Wang, Y., Chen, Y.S., Xu, X.M., Jin, Z.Y., Ding, Y.L., Yang, N., and Wu, F.F. (2017). Tuneable surface enhanced Raman spectroscopy hyphenated to chemically derivatized thin-layer chromatography plates for screening histamine in fish. Food Chem. 230, 547–552.

Yadava, S., Nairb, S.S., Saic, V.V.R., and Satijaa, J. (2019). Nanomaterials based optical and electrochemical sensing of histamine: progress and perspectives. Food Res. Int. 91, 9554–9562.

Yu, W., Freeland, D.M.H., and Nadeau, K.C. (2016). Food allergy: immune mechanisms, diagnosis and immunotherapy. Nat. Rev. Immunol. 16, 751–765.

STAR★METHODS

KEY RESOURCES TABLE

REAGENT or RESOURCE	SOURCE	IDENTIFIER
Biological samples		
Horse serum	Thermo Fisher Scientific	Cat# 26,050,070
Chemicals, peptides, and recombinant proteins		
HAuCl4·3H2O (99.9%)	Sigma-Aldrich	Cat# 520,918
Sodium silicate solution (27% SiO2)	Sigma-Aldrich	Cat# 338,443
Trisodium citrate dlhydrate (NA3C6H5O7·2H2O, 99%)	Aladdin	Cat# S116311
Histamine (96%)	Aladdin	Cat# H111796
Histamine dihydrochloride (98%)	Aladdin	Cat# H110868
Rhodamine 6G	Aladdin	Cat# R294939
Perfluoropolyether (PFPE, Fomblin Y1800)	Aladdin	Cat# F135269
3-(Trimethoxysilyl)-1-propanamine (APTMS, C6H17NO3Si, 97%)	Energy Chemical Co.	Cat# D020060
Poly tetra fluoroethylene (PTFE) membrane filter (pore size: 0.22 μm)	JINTENG Co.	NA
Critical commercial assays		
ELISA kit for histamine	Elabscience Biotechnology Co.	NA
Software and algorithms		
Gaussian package of programs	Gaussian, Inc.	NA
FDTD solutions	Lumerical Co.	NA
Other		
T64000 Raman system	National Laboratory of Solid States Microstructures and Key Laboratory of Modern Acoustics, Nanjing University,	NA

RESOURCE AVAILABILITY

Lead contact

Further information and requests for resources and reagents should be directed to and will be fulfilled by the lead contact, Xinglong Wu (hkxlwu@nju.edu.cn).

Materials availability

This study did not generate new unique reagents.

Data and code availability

All data are reported in the main text or in the supplemental information of this work. This study does not report original code.

Any additional information required to reanalyze the data reported in this paper is available from the Lead Contact upon request.

METHOD DETAILS

Raman spectral examinations

Raman spectra were obtained on a T64000 Raman system with a micro-Raman backscattering geometry at normal laser incidence, a 100× microscope objective with a numerical aperture (NA) of 0.90 was used for focusing the incident light and collecting the scattered Raman signal. Excitation source is the 514.5 nm line of an argon ion laser. The theoretical spot size was 697.4 nm based on the Abbe diffraction limit (i.e. $d = 1.22\lambda/NA$) and the power illuminating the sample was about 5 mW. The acquisition time of each Raman

spectrum was 30 s unless otherwise stated. All the measurements were conducted at room temperature without the polarization configuration. We used R6G molecules to give a standard band (1360 cm^{-1}) which changed the intensity in linear proportion to the molecular concentration (Figure S15B). This ensures to get the absolute intensities of different histamine samples.

3D-FDTD numerical method

We employed the finite-different time-domain (FDTD) method to numerically study the distribution of hot spots in a concentrated Au@SiO$_2$ NPs aggregate. We adopted 5 layers of Au@SiO$_2$ NPs with a close-packed structure to simulate cross section of the aggregate. The laser beam (514.5 nm) illuminates the layer along the z-direction. To ensure convergence of the calculation, the simulation time was set to 1,000 fs. The size of mesh in x, y, and z directions were 90 nm and the Yee cell size in all regions was $0.05 \times 0.05 \times 0.05$ nm^3. The frequency-dependent dielectric constants of Au and SiO$_2$ were taken from a multi-coefficient fitting model offered by Lumerical FDTD. Electric field distribution shows that the hot spots are mainly located around the gap between the particles in the first layer (Figure S18).

Computational details

The continuum model was employed for the solute-solvent electrostatic interaction (Mennucci et al., 2002). In this model, the liquid was assimilated to a continuum characterized by a dielectric constant 78.4 for water. All calculations were carried out using the hybrid functional B3LYP and the 6-311G** basis set under Gaussian package of programs was employed (Podstawka-Proniewicz et al., 2011). For consideration of continuum solvent effects, an extra link was added (Weijo et al., 2010). Non-electrostatic contributions to the solvation free energy (dispersion/repulsion and cavitation) were calculated on the optimized structures according to the procedure of Tomasi *et al.* implemented in Gaussian98 (Barone et al., 1998). Raman intensity was calculated depending upon the incident light frequency and temperature (Chen et al., 2019):

$$I_i = C(v_o - c_i)^4 S_i \Big/ v_i \big(1 - e^{-hcv_i/kt}\big),$$

where S_i, I_i and v_i denote the Raman activity, Raman intensity and vibration frequency (wavenumber) of the i-th vibration mode, respectively. v_o is the incident light frequency (wavenumber). *T* denotes the temperature, *h* is Planck's constant and *k* is Boltzmann's constant. The potential energy surface was obtained by scanning the dihedral angles of two carbon bonds with a step length of 10°.

Syntheses of Au NPs with different sizes and associated Au@SiO$_2$ NPs

Au NPs with different diameters were synthesized based on a citrate reduction approach. 100 mL of 0.01% (wt/Vol) aqueous HAuCl$_4$ solution was added into a round-bottom, and boiled with stirring. Add 3-8 mL of sodium citrate (1 wt%) quickly into the boiling solution. Keep boiling and stirring, the solution turned to wine red color in 10 min. After 30 min, the solution would completely react. Then colloidal Au NPs with diameters ranging from 10 to 25 nm were obtained and stored at 4°C. Add 30 mL of the colloidal Au NPs and 0.4 mL of APTMS (1 mM) into a round-bottom flask, stirring for 15 min. Dilute sodium silicate with water to 0.54% (wt/wt) and adjust the solution to pH ~10.2 with hydrochloric acid (0.01 M). Add 3.2 mL of sodium silicate solution and stir for 3 min. Oil bath at 90°C for 15 min and then stopping reaction with ice bath. Centrifuge the obtained product at 7000 rpm for 15 min and remove the supernatant and re-disperse with water. Repeat this process three times to ensure that excess reactants were removed, and clean Au@SiO$_2$ NPs were obtained and then stored in 4°C. TEM images and ultraviolet-visible (UV-vis) absorption spectra are shown in Figures S9 and S12.

Preparation of omniphobic substrates

Surface-enhanced Raman scattering (SERS) substrate was composed of Au@SiO$_2$ NPs and an omniphobic surface substrate. 0.5 mL PFPE was drip onto the PTFE membrane filter, and spun at low speed of 500 rpm for 10 s and then at high speed of 1000 rpm for 1 min to remove the excess lubricant. So, an omniphobic surface substrate was obtained successfully. 30 μL of analyte and 10 μL of the Au@SiO$_2$ NPs were mixed and then dripped onto the omniphobic substrate surface. After heated at 90°C for 10 min, the miscible liquid was concentrated to form a small aggregate because of a low friction of the omniphobic substrate surface. Optical images of the concentrated Au@SiO$_2$ NPs aggregates on the omniphobic substrates at different temperatures are shown in Figure S10. The omniphobic substrates is also effective for biological samples. Evolution of the contact angle images of the histamine/serum/Au@SiO$_2$ NP mixture during the evaporation at 90°C are shown in Figure S11. Evaluations of the enhancement efficiencies on our SERS substrates by

R6G-water solutions at different R6G concentrations are shown in Figures S13–S16. SERS enhancement factor (EF) is estimated by the following formula: $EF = \frac{I_{SERS}/N_{SERS}}{I_{RS}/N_{RS}}$, here I_{SERS} and I_{RS} are the intensities of SERS and ordinary Raman, which were obtained by the average peak area at 1360 cm^{-1} of R6G molecules with concentrations of 10^{-11} M (SERS) and 10^{-5} M (ordinary Raman) (Figures S13–S16). N_{SERS} and N_{RS} are the numbers of molecules, which are detected by SERS and ordinary Raman scattering. The EF on our SERS substrate reaches 1.0×10^6. Four enhancement Raman spectra from the dried solutions (10 μL horse serum mixed with 0.01 g/L histamine and 30 μL Au@SiO$_2$, 10 μL horse serum mixed with 30 μL Au@SiO$_2$, 30 μL horse serum, and Au@SiO$_2$ NPs solution) are shown in Figure S17.

Immunoassay reagents, equipment and procedure

Enzyme linked immunosorbent assay (ELISA) was performed using Elabscience histamine kit (Elabscience Biotechnology Co. Ltd). The samples were analyzed according to the instructions reported in the manufacturer's kit manual. Histamine in the sample or standard competed with a fixed amount of histamine on the solid phase supporter for sites on the biotinylated detection Ab specific to histamine. Excess conjugate and unbound sample or standard were washed from the plate, and avidin conjugated to horseradish peroxidase (HRP) were added to each microplate well and incubated. Then a tetramethyl-benzidine (TMB) substrate solution was added to each well. The enzyme-substrate reaction was terminated by the addition of stop solution and the color change was measured by a microtiter plate spectrophotometer (BIO-RAD iMark) at a wavelength of 450 nm. The concentrations of histamine in the samples were determined by comparing the OD (optical density) value of the samples with the standard curve. The standard curve has a linear range of 10^{-6} to 10^{-4} g/L (Figure S19A). We added different concentrations of histamine to the filtered horse serum, then detected the concentration of these samples by ELISA. We compared the actual concentration of histamine with the detected concentration (Figure S19B). Due to the influence of other impurities in the serum, the linear region was reduced to the range of 5×10^{-6} to 1×10^{-4} g/L.

QUANTIFICATION AND STATISTICAL ANALYSIS

Statistical significance

All data are represented as mean $\pm$ SEM of 10 replicate experiments unless otherwise noted, and results are considered to be statistically significant when the p value below or equal to 0.05.

Detection limit calculation

The detection limit of histamine was measured with signal-to-noise ratio method. The noise intensity is obtained from the blank sample, detection limit is identified as the concentration of the sample whose signal is three times to noise.